HHS Public Access

Author manuscript

J Magn Reson Imaging. Author manuscript; available in PMC 2018 July 01.

Published in final edited form as:

J Magn Reson Imaging. 2017 July ; 46(1): 184–193. doi:10.1002/jmri.25562.

Radiomic Features for Prostate Cancer Detection on MRI Differ Between the Transition and Peripheral Zones: Preliminary Findings from a Multi-Institutional Study

Shoshana B. Ginsburg[1,*], **Ahmad Algohary**[1], **Shivani Pahwa**[2], **Vikas Gulani**[2], **Lee Ponsky**[3], **Hannu J Aronen**[4], **Peter J Boström**[5], **Maret Böhm**[6], **Anne-Maree Haynes**[6], **Phillip Brenner**[7], **Warick Delprado**[8], **James Thompson**[6], **Marley Pulbrock**[6], **Pekka Taimen**[9], **Robert Villani**[10], **Phillip Stricker**[7], **Ardeshir R. Rastinehad**[11], **Ivan Jambor**[4], and **Anant Madabhushi**[1]

[1]Department of Biomedical Engineering, Case Western Reserve University, Cleveland, Ohio [2]Department of Radiology, Case Western Reserve University, Cleveland, Ohio [3]Department of Urology, Case Western Reserve University, Cleveland, Ohio [4]Department of Diagnostic Radiology, University of Turku, Turku, Finland [5]Department of Urology, Turku University Hospital, Turku, Finland [6]Garvan Institute of Medical Research, Sydney, Australia [7]Department of Urology, St. Vincent's Hospital, Sydney, Australia [8]Douglass Hanly Moir Pathology, Sydney, Australia [9]Department of Pathology, University of Turku and Turku University Hospital, Turku, Finland [10]Department of Radiology, Hofstra North Shore-LIJ, New Hyde Park, New York [11]Department of Radiology, Icahn School of Medicine at Mount Sinai, Manhattan, New York

Abstract

Purpose—To evaluate in a multi-institutional study whether radiomic features useful for prostate cancer (PCa) detection from 3 Tesla (T) multi-parametric MRI (mpMRI) in the transition zone (TZ) differ from those in the peripheral zone (PZ).

Materials and Methods—3T mpMRI, including T2-weighted (T2w), apparent diffusion coefficient (ADC) maps, and dynamic contrast-enhanced MRI (DCE-MRI), were retrospectively obtained from 80 patients at three institutions. This study was approved by the institutional review board of each participating institution. First-order statistical, co-occurrence, and wavelet features were extracted from T2w MRI and ADC maps, and contrast kinetic features were extracted from DCE-MRI. Feature selection was performed to identify ten features for PCa detection in the TZ and PZ, respectively. Two logistic regression classifiers used these features to detect PCa and were evaluated by area under the receiver-operating characteristic curve (AUC). Classifier performance was compared with a zone-ignorant classifier.

Results—Radiomic features that were identified as useful for PCa detection differed between TZ and PZ. When classification was performed on a per-voxel basis, a PZ-specific classifier detected PZ tumors on an independent test set with significantly higher accuracy (AUC = 0.61-0.71) than a zone-ignorant classifier trained to detect cancer throughout the entire prostate (p<0.05). When

[*]Corresponding author: shoshana.ginsburg@case.edu.

classifiers were evaluated on MRI data from multiple institutions, statistically similar AUC values ($p > 0.14$) were obtained for all institutions.

Conclusions—A zone-aware classifier significantly improves the accuracy of cancer detection in the PZ.

Keywords

Magnetic resonance imaging; prostate cancer; radiomics; multi-institutional

INTRODUCTION

Prostate MRI provides excellent contrast of anatomic structures on T2-weighted (T2w) MRI, as well as diffusion characteristics and microvasculature on diffusion-weighted (DW) MRI and dynamic contrast-enhanced (DCE) MRI, respectively (1). However, up to one quarter of prostate cancers in the transition zone (TZ) might not be detected on MRI, primarily due to the presence of benign tumor confounding pathologies such as benign prostatic hyperplasia (2). Additionally, areas of benign stroma or hyperplasia may manifest as restricted diffusion on DW MRI and heterogeneous enhancement on DCE MRI (3). As a result, functional imaging (DW MRI, DCE MRI) is not necessarily useful for detecting TZ tumors.

Computer-assisted diagnosis (CAD) tools provide increased sensitivity and specificity in detecting prostate cancer on multi-parametric MRI, to complement radiologists' assessments (4). Recently there has been substantial interest in the role of computer-extracted (or radiomic) texture features to quantitatively describe tissue microarchitecture and morphology. A number of CAD approaches have used textural features, including first and second order co-occurring statistical measurements, from T2w and diffusion weighted MRI and kinetic features from DCE MRI for prostate cancer detection (4-17).

Although many CAD studies have been published over the past decade (4-17), these studies focus on imaging data from a single institution. In order for a CAD algorithm to be generally useful, however, it must be robust to differences in MR imaging parameters. This is a particularly important consideration since MR imaging parameters and scanning protocols are not standard across institutions. Furthermore, the variance (or drift) in MRI parameters (T1w, T2w, Diffusion) across vendor platforms and scanners is well-known and documented (22). Therefore, it is important to identify radiomic features and develop associated CAD algorithms that are robust to this variability induced by differences in MR imaging parameters across scanners and vendor platforms.

The prostate gland can be divided into three primary anatomical regions: the peripheral zone (PZ), the TZ, and the central zone. Prostate cancer in the central zone is rare (18). While some CAD approaches are designed to look for prostate cancer only in the PZ (7-9, 19, 20) or TZ (10, 11), many approaches tend to be zone-ignorant. However, the appearance of prostate cancer on MRI tends to depend on the tumor's location in the prostate gland (5, 6). Whereas PZ tumors usually manifest on T2w MRI as round or ill-defined hypointense lesions, TZ tumors are usually moderately hypointense, lenticular-shaped lesions, often with spiculated margins (21). Additionally, radiomic texture features extracted from T2w MRI, as

well as ADC maps and DCE MRI, for characterizing TZ tumors have been shown to be different from those characterizing PZ tumors on multi-parametric MRI (5, 6).

Although there has been some recent work on identifying zone-specific radiomic features associated with prostate cancer in the TZ and PZ (5, 6), these limited studies have been specific to a single institution, and the resilience of these features was not evaluated in a cross-institutional setting. The purpose of this work was to evaluate in a multi-institutional study whether radiomic features for prostate cancer detection from multi-parametric 3 Tesla (T) MRI in the TZ are similar to the features that are useful for prostate cancer detection in the PZ.

MATERIALS AND METHODS

Patients

This retrospective study included 87 patients from three institutions (Turku University Hospital, Turku, Finland; St. Vincent's Hospital, Sydney, Australia; and Mt. Sinai Hospital, New York, USA) and was approved by the institutional review board of each institution. Patients from Turku University were part of a previously completed prospective study (23) or were enrolled in an ongoing prospective clinical trial (Clinical Trial registration: NCT02002455). All patients underwent multi-parametric MRI due to suspicion for prostate cancer either prior to prostate biopsy (52 patients) (23) or prior to radical prostatectomy (35 patients). Five patients from the former group were excluded due to poor quality of MRI, and two patients were excluded because complete multi-parametric MRI was not performed. Whole-mount prostatectomy specimens were also available for the 35 patients who underwent radical prostatectomy following MRI, as well as 18 patients who underwent pre-biopsy MRI but subsequently underwent radical prostatectomy. Thus, a total of 80 patients were included (age range, 40-79 years; median, 64 years); radical prostatectomy specimens were available for 51 of these patients. Further details regarding the patients included in this study can be found in Table 1.

MRI Acquisition

MRI was performed with a 3-Tesla MR scanner either with a body coil (67 patients) or an endorectal coil (13 patients). The multi-parametric MRI protocol consisted of T2-weighted imaging, diffusion-weighted imaging, and dynamic contrast-enhanced imaging. MRI acquisition details are listed in Table 1.

Histopathological Analysis and Cancer Annotation on MRI

For subjects from Turku University who underwent radical prostatectomy following MRI acquisition, whole mount prostatectomy sections were obtained, processed as described in (24), and stained with hematoxylin and eosin. All of the histopathologic material was analyzed by one genitourinary pathologist (8 years of experience in genitourinary pathology) in consensus with another pathologist (6 years of experience in genitourinary pathology). The Gleason score was assigned as a combination of primary, secondary, and tertiary Gleason grades according to the 2005 International Society of Urological Pathology Modified Gleason Grading System (25). A tertiary Gleason grade was assigned when a

Gleason grade pattern higher than the primary and secondary Gleason grade patterns was present but accounted for less than 5% of the tumor (26). Following histopathological analysis, the histologic slides (50×75 mm^2) were digitized in 2400 dpi resolution using a high resolution scanner.

In order to obtain "ground truth" annotation of prostate cancer extent on MRI, deformable co-registration of MRI and whole mount histological sections was performed. Correspondences between histological sections and T2w MRI slices were determined by a genitourinary pathologist and radiologist working in unison. Subsequently, corresponding histological sections and MRI slices were co-registered using an interactive B-spline elastic registration scheme (27). The final result was a labeling of each MRI voxel within the prostate as corresponding to cancer or benign prostate tissue.

Cancer Annotation on Pre-Biopsy MRI

For the 29 subjects who did not undergo radical prostatectomy following MRI acquisition, ground truth for prostate cancer extent from excised surgical histopathology was not available. These included 16 subjects from St. Vincent's Hospital and 13 subjects from Mt. Sinai Hospital. For the subjects from St. Vincent's, a genitourinary radiologist (9 years of experience) assessed multi-parametric MRI for cancer presence and annotated prostate cancer extent, if present, on T2w MRI. For the subjects from Mt. Sinai, a genitourinary radiologist (5 years of experience) annotated the extent of visible cancer on T2w MRI within sextants associated with positive biopsy results. All lesions were correlated with fusion targeted biopsy results.

MRI Post-Processing

DCE MRI and ADC maps (24) obtained from DWI were spatially aligned with T2w MRI via volumetric affine registration, which corrected inter-acquisition movement and inter-protocol resolution differences. After inter-protocol alignment, all MRI data from all institutions were computationally analyzed at the T2w MRI resolution of $0.625 \times 0.625 \times 3$mm^2. The prostate capsule and TZ were manually annotated on T2w MRI by a radiologist with 7 years of experience in prostate MRI. Finally, T2w and DCE MRI were corrected for acquisition-based MRI intensity artifacts (28). We first corrected for intensity inter- and intra-patient T2w MRI "intensity drift", which causes T2w MRI intensities to lack tissue-specific numeric meaning (22). This effect was corrected by interactive implementation of the generalized scale algorithm (22), which aligns image intensity histograms across different MRI studies, thereby enabling MRI intensities to have a consistent tissue-specific numeric meaning. Additionally, for patients who were imaged using an endorectal probe, the bias field artifact occurring on T2w and DCE MRI was corrected by the N3 algorithm (29).

Radiomic Features

Our feature set included signal intensities on T2w MRI, ADC values, and six kinetic features describing the uptake and washout of contrast on DCE MRI (see Table 2). In addition, 224 radiomic features (see Table 2), including first-order statistical, co-occurrence, and wavelet features computed from both T2w MRI and ADC maps, were extracted. These features are designed to accentuate smooth and spiculated margins and to differentiate between

homogeneous regions of low signal intensity associated with prostate cancer and surrounding normal prostate tissue.

Identifying Features for Discriminating Cancerous from Benign Voxels

Radiomic features were selected based on (a) resilience and lack of variability between patients and institutions and (b) ability to discriminate between cancerous and benign prostate voxels. Feature resilience across patients and institutions was determined based on Cronbach's intra-class correlation coefficient (ICC) (30), which measures the level of concordance in feature values. Features associated with an ICC > 0.9 were considered resilient to inter-patient and inter-institutional differences. For each feature identified as resilient, binary logistic regression was implemented to classify individual voxels as cancerous or benign, and the area under the receiver-operating characteristic (ROC) curve (AUC) was calculated based on the posterior probabilities of a voxel being classified as cancerous. Finally, features associated with both the highest AUC values and ICC > 0.9 were identified as being useful for characterizing prostate cancer in a multi-institutional setting. Two separate sets of features were identified: one set of features that characterize TZ cancers (F^{TZ}) and another set of features to characterize PZ cancers (F^{PZ}). Additionally, a third set of features was identified that did not specifically consider zonal anatomy (F^{ALL}). Separate radiomic feature sets were obtained based on patients from Turku University (I_1), patients from St. Vincent's (I_2), and the combination of patients who underwent radical prostatectomy from Turku University and St. Vincent's ($I_{12} = I_1 \cup I_2$). Thus, nine separate feature sets were obtained: F_1^{TZ}, F_2^{TZ}, F_{12}^{TZ}, F_1^{PZ}, F_2^{PZ}, F_{12}^{PZ}, F_1^{ALL}, F_2^{ALL}, and F_{12}^{ALL}. Note that only feature sets F_{12}^{TZ}, F_{12}^{PZ}, and F_{12}^{ALL} were selected based on resilience to inter-patient and inter-institutional differences, while the other feature sets were selected based on resilience to inter-patient differences only.

Classifier Training and Evaluation

For each training set, two separate logistic regression classifiers (31) were trained: one used F^{TZ} to detect cancer in the TZ (C^{TZ}) and the other used F^{PZ} to detect cancer in the PZ (C^{PZ}). For comparison, a zone-ignorant classifier (C^{ALL}) that leveraged F^{ALL} to detect cancer across the entire prostate was also trained and evaluated. The performance of C^{TZ}, C^{PZ}, and C^{ALL} was evaluated by the AUC. In order to keep training and testing populations separate from each other, separate classifiers were trained using each feature set: C_1^{TZ}, C_2^{TZ}, C_{12}^{TZ}, C_1^{PZ}, C_2^{PZ}, C_{12}^{PZ}, C_1^{ALL}, C_2^{ALL}, and C_{12}^{ALL} based on F_1^{TZ}, F_2^{TZ}, F_{12}^{TZ}, F_1^{PZ}, F_2^{PZ}, F_{12}^{PZ}, F_1^{ALL}, F_2^{ALL}, and F_{12}^{ALL}. Each of these classifiers was trained in a leave-one-out cross-validation scheme and evaluated in terms of its ability to detect prostate cancer on MRI obtained from an independent institution (e.g., C_1^{TZ} and C_1^{PZ} were evaluated on data from St. Vincent's and Mt. Sinai, and C_2^{TZ} and C_2^{PZ} were evaluated on data from Turku University and Mt. Sinai). Additionally, correlations between AUC values representing cancer detection accuracy and Gleason scores associated with prostate cancer lesions were assessed via Spearman's correlation coefficient.

RESULTS

Differences in Radiomic Features between TZ and PZ Classifiers

The top ten radiomic features selected for detecting TZ and PZ tumors are listed in Table 3. The features in F_1^{PZ} and F_{12}^{PZ} included a combination of Gabor wavelet features, co-occurrence features, and edge descriptors extracted from T2w MRI, whereas F_2^{PZ} included only co-occurrence features. Only two of the features in F_1^{PZ}, and none in F_2^{PZ} or F_{12}^{PZ} were based on ADC maps; no features extracted from DCE MRI were included in F^{PZ}. Gabor wavelet features, co-occurrence features, and edge descriptors extracted from T2w MRI were useful for detecting TZ cancer, too. Unlike for F^{PZ}, however, each of F_1^{TZ}, F_2^{TZ}, and F_{12}^{TZ} included 1-6 features computed from ADC maps. The top ranked Gabor wavelet and co-occurrence features in F_{12}^{TZ} and F_{12}^{PZ} are shown in Figure 1.

The features in F^{ALL} corresponded more closely with the features in F^{PZ} than F^{TZ}. In particular, 3/10 features were common to both F_1^{ALL} and F_1^{PZ}, 2 co-occurrence features (sum variance and information measure 1) were common to both F_2^{ALL} and F_2^{PZ}, and 9/10 features were identical between F_{12}^{ALL} and F_{12}^{PZ}. By contrast, two Gabor features were common to both F_1^{ALL} and F_1^{TZ}, two Kirsch edge descriptors were identical between F_{12}^{ALL} and F_{12}^{PZ}, and F_2^{ALL} and F_2^{PZ} did not intersect at all.

Classifier Performance

When applied to detect PZ cancer on the studies in I_1 and I_2, C_1^{PZ}, C_2^{PZ}, and C_{12}^{PZ} yielded AUC values ranging between 0.61 and 0.71, although these classifiers yielded lower AUC values when applied to studies in I_3 (0.54-0.58; see Table 4). C_1^{PZ}, C_2^{PZ}, and C_{12}^{PZ} detected PZ cancer with higher AUC than C_1^{ALL}, C_2^{ALL}, and C_{12}^{ALL}, respectively. The difference in AUC between C_1^{PZ} and C_1^{ALL}, as well as between C_2^{PZ} and C_2^{ALL}, was statistically significant ($p < 0.05$). C_1^{TZ}, C_2^{TZ}, and C_{12}^{TZ} detected prostate cancer in the TZ on a per-voxel level with AUC values ranging between 0.54 and 0.68, and C_1^{ALL}, C_2^{ALL}, and C_{12}^{ALL} yielded statistically similar AUC values (0.53-0.66; see Table 4). There were no statistically significant differences in AUC values between C^{ALL} and C^{TZ}.

Correlation with Gleason Scores

When C_{12}^{TZ} was applied for cancer detection on MRI from I_1, AUC values correlated poorly with Gleason scores ($\rho = 0.05$, see Figure 2(a)). When C_{12}^{PZ} was applied for cancer detection on MRI from I_1, AUC values correlated somewhat with Gleason scores ($\rho = 0.16$, see Figure 2(b)).

Effect of Training Cohort on Classifier Performance

A two-sample Student's t-test was used to evaluate whether statistically significant differences existed between AUC values yielded by C_1^{TZ}, C_2^{TZ}, and C_{12}^{TZ}, as well as between

C_1^{PZ}, C_2^{PZ}, and C_{12}^{PZ}. When applied to detect cancer on the studies in I_1, I_2, and I_3, C_1^{PZ}, C_2^{PZ}, and C_{12}^{PZ} yielded statistically similar AUC values ($p > 0.14$ for TZ cancer and $p > 0.56$ for PZ cancer).

Differences Between Small and Large Tumors

A two-sample Student's *t*-test was used to evaluate whether both small (< 0.5 cm^3 or < 1 cm^3 on T2w MRI) and large tumors (> 1 cm^3 on T2w MRI) share the same characteristics on multi-parametric MRI. After Bonferroni correction for the effect of multiple testing, there were no significant differences between small and large tumors. Cancer detection improved with tumor size, as AUC values were somewhat correlated with tumor size ($\rho = 0.14$, see Figure 2(c)). Five small tumors from I_1 that were <1 cm^3 were associated with high Gleason scores (>7) and were therefore clinically significant. These tumors ranged in size from 0.35-0.5 cm^3. Four of these tumors were associated with AUC values ranging between 0.58-0.79, while one was associated with an AUC value below 0.5. Of nine tumors smaller than 0.2 cm^3 (considered the limit for tumor visibility on MRI), four were detected with an AUC ranging between 0.65-0.83, while the remaining five were associated with AUC values below 0.5.

DISCUSSION

In this study we identified and evaluated radiomic features associated with TZ and PZ tumors on multi-parametric MRI. We found that distinct sets of radiomic features were useful for cancer detection in the TZ and PZ, respectively. Furthermore, the cancer detection accuracy associated with these features was not significantly different across the three institutions considered in this study.

Regardless of training cohort, F^{TZ} and F^{PZ} did not overlap at all. This finding suggests that multi-parametric MRI radiomic features identified as useful for cancer detection in the PZ were distinct from radiomic features that are useful for cancer detection in the TZ. Our findings indicate the importance of Gabor wavelet features, co-occurrence texture features, and edge descriptors for distinguishing prostate cancer from benign prostate tissue in the TZ and the PZ. The multiscale, steerable Gabor wavelets that were dominant in F^{TZ} regardless of training cohort appear to model localized frequency characteristics, thereby distinguishing between the hypo-intense, homogeneous texture of TZ tumors and the more heterogeneous surrounding normal TZ tissue. The co-occurrence features, which dominate F_2^{PZ} and play roles in F_1^{PZ} and F_{12}^{PZ} have previously been found to be particularly useful for distinguishing between hypo-intense PZ cancer and hyper-intense normal PZ tissue (6). The dearth of ADC and DCE features in F^{PZ} and F^{TZ} may be related to DWI and DCE MRI data quality.

Accounting for differences between TZ and PZ tumors by identifying unique feature sets F^{TZ} and F^{PZ} and subsequently developing distinct classifiers C^{TZ} and C^{PZ} led to significantly improved cancer detection in the PZ. C^{PZ} yielded voxel-wise AUC values as high as 0.71, whereas C^{ALL} performed no better than random guessing (AUC ≤ 0.51). In contrast to the PZ, in the TZ C^{TZ} and C^{ALL} performed similarly to each other, providing AUC values ranging between 0.54-0.68. This result may possibly be due to the inherent

difficulty in distinguishing between tumors in the TZ and confounding disease, such as benign prostatic hyperplasia, that manifests predominantly in the TZ.

The AUC values associated with C^{TZ} and C^{PZ} were lower than those obtained in other studies [4, 5], which reported voxel-wise AUC values as high as 0.73-0.86 for cancer detection in the PZ and/or TZ. However, the results reported in (5, 6) were all based on cross-validation within a single institution. Our lower AUC could possibly be attributed to the fact that 75% of the tumors in our cohort were < 1 cm^3 in size. Nevertheless, 80% of small tumors that were clinically significant (Gleason score > 7) were detected on MRI. The AUC values correlated somewhat with tumor size, as larger tumors were associated with higher AUC values (see Figure 2(c)). The correlation between Gleason scores and AUC values for all tumors from I_1 was poor in both the TZ and PZ (see Figures 2(a), 2(b)). This is not surprising since the classifiers were trained to discriminate between prostate cancer and benign tissue; they were not trained to distinguish between cancer grades.

Our study did have its limitations. Firstly, this was a multi-institutional study. While this was a unique aspect of our study, it was also a limitation because the MRI acquisition parameters (e.g., *b*-values for acquiring diffusion-weighted MRI, temporal resolution of DCE MRI) differed between institutions. This lack of consistency may explain why primarily T2-weighted MRI features were chosen during feature selection, whereas most ADC- and DCE-based features were not highly ranked by our feature selection scheme. Nevertheless, our study demonstrated that radiomic features can be effective for prostate cancer detection even in the face of variability in image acquisition parameters. Secondly, whereas the MRI data from I_1 and I_2 was acquired using a body coil, the MRI data from I_3 was acquired using an endorectal coil. This may have contributed to the lower cancer detection accuracy associated with I_3, particularly in the PZ, where the effect of the endorectal coil would be most seen. Finally, for 29 subjects in our cohort, ground truth prostate cancer extent on pathology was not available. For 13 of these subjects, prostate cancer extent was annotated on MRI based on correlation with fusion targeted biopsy results, but for the remaining 16 subjects a genitourinary radiologist annotated prostate cancer extent based on visual assessment of multi-parametric MRI alone. In the absence of pathology fused with MRI, it was not possible to be certain of the exact extent of prostate cancer for these cases.

In conclusion, the radiomic features identified as useful for cancer detection in the PZ were different from those that were useful for TZ cancers. These features were evaluated cross-institutionally and found to be useful for prostate cancer detection on MRI from three institutions. Our finding that a zone-aware classifier significantly improves the accuracy of cancer detection in the PZ suggests that decision support tools for evaluating prostate MRI exams should take into account differences between TZ and PZ tumors.

Acknowledgments

Funding agencies: This work was made possible by grants from the National Science Foundation Graduate Research Fellowship; the National Cancer Institute of the National Institutes of Health under award numbers R01CA136535-01, R01CA140772- 01, R21CA167811-01, R21CA179327-01, R21CA195152-01; the National Institute of Diabetes and Digestive and Kidney Diseases under award number R01DK098503-02; the DOD Prostate Cancer Synergistic Idea Development Award (PC120857); the DOD Lung Cancer Idea Development New Investigator Award (LC130463); the DOD Prostate Cancer Idea Development Award; the Ohio Third Frontier

Technology development Grant; the CTSC Coulter Annual Pilot Grant; the Case Comprehensive Cancer Center Pilot Grant; VelaSano Grant from the Cleveland Clinic; the Wallace H. Coulter Foundation Program in the Department of Biomedical Engineering at Case Western Reserve University; and the Academy of Finland.

Appendix I: Radiomic Feature Descriptions

Texture Features

Texture features, including first-order statistics, co-occurrence features, Gabor and Haar wavelet features, and edge descriptors were calculated based on both T2w MRI and ADC maps. Parameter settings for these features, which are described below, are listed in Table 2.

First-order statistics [32]: Mean, standard deviation, and range of intensities

Co-occurrence features [33]: Statistical features computed from the join probability distribution of intensity value co-occurrences

Gabor wavelet features [34]: Multi-orientation features computed from a Gaussian function convolved with a sinusoid

Haar wavelet features [35]: Multi-level coefficients from a Haar wavelet decomposition

Edge descriptors [32]: Non-steerable gradient features obtained by convolution with Sobel and Kirsch operators

Pharmacokinetic Features

Time to Peak: The interval between the pre-contrast time point and post-contrast time point at which the lesion achieved maximum signal intensity

Maximum uptake: The signal intensity associated with the time to peak

Uptake rate: The rate of change in signal intensity over the interval between the first time point and the time to peak

Washout rate: The rate of change in signal intensity over the interval between the time to peak and the time point at which lowest signal enhancement is achieved

Enhancement: The signal intensity at the first post-contrast time point

Enhancement ratio: The ratio of enhancement to maximum uptake

REFERENCES

1. Schimmoller L, Quentim M, Arsov C, et al. MR-sequences for prostate cancer diagnostics: Validation based on the PIRADS scoring system and targeted MR-guided in-bore biopsy. Eur Radiol. 2014; 24(10):2582–2589. [PubMed: 24972954]
2. Kayhan A, Fan X, Oommen J, Oto A. Multi-parametric MR imaging of transition zone prostate cancer: Imaging features, detection and staging. World J Radiol. 2010; 2(5):180–187. [PubMed: 21161033]

3. Hoeks CM, Vos EK, Bomers JG, et al. Diffusion-weighted magnetic resonance imaging in the prostate transition zone: Histopathological validation using magnetic resonance-guided biopsy specimens. Invest Radiol. 2013; 48(10):693–701. [PubMed: 23614975]
4. Hambrock T, Vos PC, Hulsbergen-van de Kaa CA, et al. Prostate cancer: Computer-aided diagnosis with multi-parametric 3-T MR imaging—effect on observer performance. Radiology. 2013; 266:521–530. [PubMed: 23204542]
5. Ginsburg SB, Viswanath SE, Bloch BN, et al. Novel PCA-VIP scheme for ranking MRI protocols and identifying computer-extracted MRI measurements associated with central gland and peripheral zone prostate tumors. J Magn Reson Imaging. 2015; 41(5):1383–1393. [PubMed: 24943647]
6. Viswanath SE, Bloch BN, Chappelow JC, et al. Central gland and peripheral zone prostate tumors have significantly different quantitative imaging signatures on 3 Tesla endorectal, in vivo T2-weighted MR imagery. J Magn Reson Imaging. 2012; 36(1):213–224. [PubMed: 22337003]
7. Vignati A, Mazzetti S, Giannini V, et al. Texture features on T2-weighted magnetic resonance imaging: New potential biomarkers for prostate cancer aggressiveness. Phys Med Biol. 2015; 60(7): 2685–2701. [PubMed: 25768265]
8. Garcia Molina JF, Zheng L, Sertdemir M, et al. Incremental learning with SVM for multimodal classification of prostatic adenocarcinoma. PLoS One. 2014; 9(4):e93600. [PubMed: 24699716]
9. Niaf E, Rouviere O, Mege-Lechevallier F, et al. Computer-aided diagnosis of prostate cancer in the peripheral zone using multiparametric MRI. Phys Med Biol. 2012; 57:3833–3851. [PubMed: 22640958]
10. Stember JN, Deng FM, Taneja SS, Rosenkrantz AB. Pilot study of a novel tool for input-free automated identification of transition zone prostate tumors using T2- and diffusion-weighted signal and textural features. J Magn Reson Imaging. 2014; 40(2):301–305. [PubMed: 24924512]
11. Dikaios N, Alkalbani J, Sidhu HS, et al. Logistic regression model for diagnosis of transition zone prostate cancer on multi-parametric MRI. Eur Radiol. 2015; 25:523–532. [PubMed: 25226842]
12. Kwak JT, Xu S, Wood BJ, et al. Automated prostate cancer detection using T2-weighted and high-b-value diffusion-weighted magnetic resonance imaging. Med Phys. 2015; 42:2368. [PubMed: 25979032]
13. Litjens GJS, Elliott R, Shih N, et al. Computer-extracted features can distinguish noncancerous confounding disease from prostatic adenocarcinoma at multiparametric MR imaging. Radiology. 2016; 278(1):135–145. [PubMed: 26192734]
14. Khalvati F, Wong A, Haider MA. Automated prostate cancer detection via comprehensive multi-parametric magnetic resonance imaging texture feature models. BMC Med Imaging. 2015; 15:27. [PubMed: 26242589]
15. Wibmer A, Hricak H, Gondo T, et al. Haralick texture analysis of prostate MRI: utility for differentiating non-cancerous prostate from prostate cancer and differentiating prostate cancers with different Gleason scores. Eur Radiol. 2015; 25(10):2840–2850. [PubMed: 25991476]
16. Singanamalli A, Rusu M, Sparks RE, et al. Identifying in vivo DCE MRI markers associated with microvessel architecture and Gleason grades of prostate cancer. Journal of Magnetic Resonance Imaging. 2016; 43(1):149–158. [PubMed: 26110513]
17. Metzger GJ, Kalavagunta C, Spilseth B, et al. Detection of prostate cancer: Multiparametric MR imaging models developed by using registered correlative histopathologic results. Radiology. 2016 Available online.
18. Cohen RJ, Shannon BA, Phillips M, et al. Central zone carcinoma of the prostate gland: a distinct tumor type with poor prognostic features. Journal of Urology. 2008; 179(5):1762–1767. [PubMed: 18343454]
19. Shah V, Turkbey B, Mani H, et al. Decision support system for localizing prostate cancer based on multiparametric magnetic resonance imaging. Med Phys. 2012; 39:4093–4103.
20. Peng Y, Jiang Y, Antic T, et al. Validation of quantitative analysis of multiparametric MR images for prostate cancer detection and aggressiveness assessment: a cross-imager study. Radiology. 2014; 271(2):461–471. [PubMed: 24533870]
21. Turkbey B, Bernardo M, Merino MJ, et al. MRI of localized prostate cancer: Coming of age in the PSA era. Diagnostic Interventional Radiology. 2012; 18:34–45. [PubMed: 21922459]

22. Madabhushi A, Udupa JK. New methods of MR image intensity standardization via generalized scale. Med Phys. 2006; 33:3426–3434. [PubMed: 17022239]
23. Jambor I, Kahkonen E, Taimen P, et al. Prebiopsy multiparametric 3T prostate MRI in patients with elevated PSA, normal digital rectal examination, and no previous biopsy. J Magn Reson Imaging. 2015; 41:1394–1404. [PubMed: 24956412]
24. Jambor I, Pesola M, Taimen P, et al. Rotating frame relaxation imaging of prostate cancer: Repeatability, cancer detection, and Gleason score prediction. Magn Reson Med. 2015
25. Epstein JI, Allsbrook WC Jr, Amin MB, Egevad LL. The 2005 International Society of Urological Pathology (ISUP) Consensus Conference on Gleason Grading of Prostatic Carcinoma. Am J Surg Pathol. 2005; 29:1228–1242. [PubMed: 16096414]
26. Epstein JI. An update of the Gleason grading system. J Urol. 2010; 183:433–440. [PubMed: 20006878]
27. Chappelow J, Bloch BN, Rofsky N, et al. Elastic registration of multimodal prostate MRI and histology via multiattribute combined mutual information. Med Phys. 2011; 38:2005–2018. [PubMed: 21626933]
28. Madabhushi A, Feldman MD, Metaxas DN, et al. Automated detection of prostatic adenocarcinoma from high-resolution ex vivo MRI. IEEE Trans Med Imaging. 2005; 24:1611–1625. [PubMed: 16350920]
29. Sled JG, Zijdenbos AP, Evans AC. A nonparametric method for automatic correction of intensity nonuniformity in MRI data. IEEE Trans Med Imaging. 1998; 17:87–97. [PubMed: 9617910]
30. Cronbach LJ. Coefficient alpha and the interval structure of tests. Psychometrika. 1951; 16:297–334.
31. Hastie, T., Tibshirani, R., Friedman, J. The elements of statistical learning: data mining, inference, and prediction. Spring; New York: 2001.
32. Russ, JC. The Image Processing Handbook. CRC Press; New York: 2007.
33. Haralick RM, Shanmugan K, Dinstein IH. Textural features for image classification. IEEE Transations on Sytems, Man and Cibernetics. 1973; 3:610–621.
34. Bovik AC, Clark M, Geisler WS. Multichannel texture analysis using localized spatial filters. IEEE Transactions on Pattern Analysis and Machine Intelligence. 1990; 12:55–73.
35. Busch C. Wavelet based texture segmentation of multi-modal tomographic images. Computers and Graphics. 1997; 21:347–358.

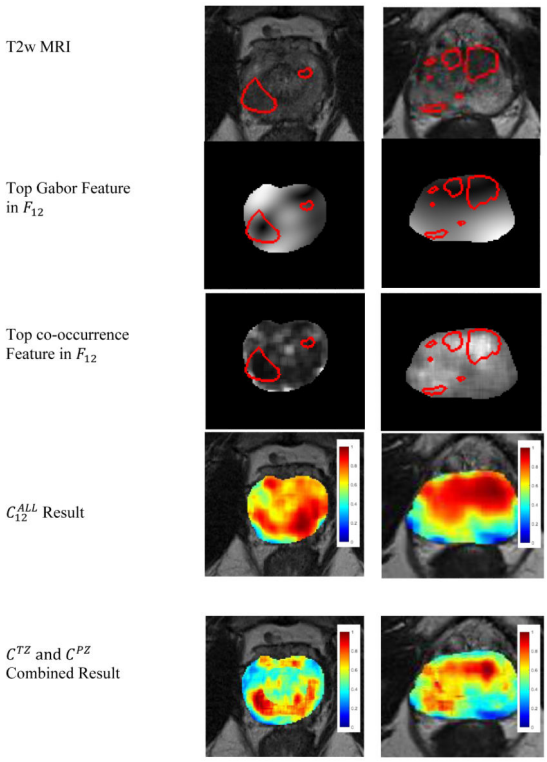

Figure 1.

Ground truth extent of prostate cancer is delineated on T2w MRI in red for a representative slice of (left) a PZ tumor and (right) a TZ tumor. Feature maps of the top two selected features populating F_{12}^{PZ} and F_{12}^{TZ}, respectively, are also shown. Heatmaps representing the pixel-wise probability of cancer presence, obtained via logistic regression classifiers trained on data from Turku University and St. Vincent's, are shown when C_{12}^{ALL} is used and when C_{12}^{PZ} and C_{12}^{TZ} complement each other to detect cancer in both the PZ and TZ. Red indicates a high probability of cancer presence, yellow indicates a low probability of cancer presence, and blue, the absence of cancer.

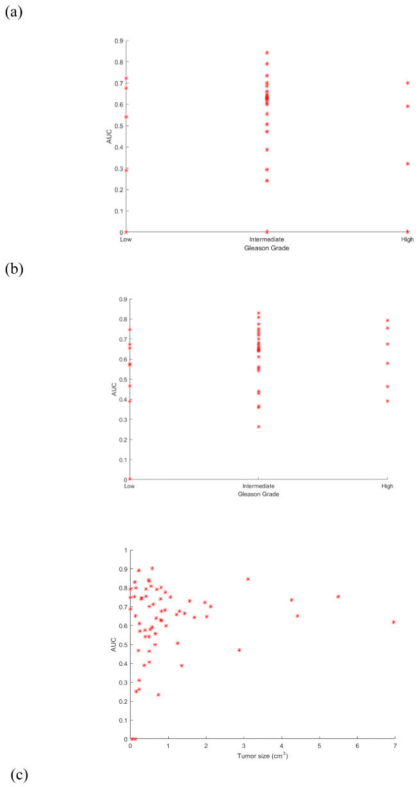

Figure 2.

Scatterplot of areas under receiver operating characteristic curve (AUCs) yielded by the spatially-aware classifier on a per-patient basis versus (a) Gleason scores for patients from St. Vincent's with TZ tumors, (b) Gleason scores for patients from St. Vincent's with PZ tumors, and (c) overall tumor sizes for all 80 patients.

Table 1

Description of subjects used in this study

	Turku University	St. Vincent's	Mt. Sinai
# subjects	40	27	13
Scanner	Siemens Verio	Philips Achieva	Siemens Verio
Magnet strength	3T	3T	3T
Coil type	Body coil	Body coil	Endorectal coil
T2-weighted MRI			
Field-of-view	200 × 200 mm^2	220 × 220 mm^2	140 × 140 mm^2
Matrix size	320 × 320	444 × 332	384 × 384
Slice thickness	3 mm	3 mm	3 mm
DW MRI			
Field-of-view	260 × 260 mm^2	180 × 180 mm^2	260 × 186 mm^2
Matrix size	128 × 128	128 × 128	116 × 162
Slice thickness	3 mm	3 mm	3 mm
b-values	0, 100, 200, 350, 500 s/mm^2	0, 1500 s/mm^2	0, 2000 s/mm^2
DCE MRI			
Field-of-view	240 × 240 mm^2	200 × 200 mm^2	250 × 250 mm^2
Matrix size	192 × 192	128 × 128	192 × 192
Slice thickness	3 mm	3 mm	3 mm
Flip angle	15°	8°	12°
Temporal resolution	6.9 sec	5.5 sec	5 sec
n time points	60	50	45
Age (mean±SD)	64.3±5.6	65.1±6.4	62.6±10.8
PSA (mean±SD)	9.8±6.3	6.9±5.8	5.9±4.2
Lesion size (mean±SD)	1.02±1.16 cm^3	1.10±1.79 cm^3	0.67±0.82 cm^3
Zone containing lesions	23 TZ, 35 PZ	6 TZ, 24 PZ	8 TZ, 11 PZ
Gleason scores			
Low (≤6)	8	-	NA
Intermediate (7)	26	9	NA
High (≥8)	6	2	NA

DW, diffusion-weighted; DCE, dynamic contrast enhanced; SD, standard deviation

Table 2

Overview of radiomic texture features used in this study

Features	Pulse Sequence	Parameters
Signal Intensities		
T2-weighted	Axial T2-weighted	-
ADC	Diffusion-weighted	-
Texture		
First-order statistics [32]	T2-weighted, ADC	-
Co-occurrence features [33]	T2-weighted, ADC	w = 3,5,7
2D multi-angle Gabor [34]	T2-weighted, ADC	θ = 0-2.75, λ = 2.8-45.3
Haar wavelet [35]	T2-weighted, ADC	4 levels
Edge descriptors [32]	T2-weighted, ADC	-
Kinetic		
Time-to-peak	DCE	-
Initial enhancement	DCE	-
Maximum enhancement	DCE	-
Enhancement ratio	DCE	-
Uptake rate	DCE	-
Washout rate	DCE	-

Table 3

Top ten radiomic features selected based on an intraclass correlation coefficient above 0.9 and high AUC values in distinguishing prostate cancer and benign tissue. Features extracted from ADC maps are shown in bold font.

$F_{1,2}^{PZ}$	F_{1}^{PZ}	F_{2}^{PZ}
Difference entropy ($w = 5$)	Sum variance ($w = 3$)	Sum variance ($w = 5$)
Gabor ($\theta = 1.12$, $\lambda = 22.6$)	**Gabor ($\theta = 0.79$, $\lambda = 2.8$)**	Sum entropy ($w = 5$)
Gabor ($\theta = 0.39$, $\lambda = 22.6$)	**Gabor ($\theta = 0$, $\lambda = 5.7$)**	Sum variance ($w = 7$)
Gabor ($\theta = 2.36$, $\lambda = 22.6$)	Gabor ($\theta = 1.96$, $\lambda = 11.3$)	Sum entropy ($w = 7$)
Info. measure 1 ($w = 7$)	Kirsch edge descriptor 3	Sum average ($w = 5$)
Energy ($w = 3$)	Kirsch edge descriptor 1	Info. measure 1 ($w = 5$)
Kirsch edge descriptor 3	Energy ($w = 7$)	Diff. variance ($w = 5$)
Kirsch edge descriptor 2	Kirsch edge descriptor 2	Sum average ($w = 3$)
Gabor ($\theta = 2.36$, $\lambda = 8.2$)	Gabor ($\theta = 0.79$, $\lambda = 8.2$)	Info. measure 1 ($w = 3$)
T2w MRI intensity	Gabor ($\theta = 1.58$, $\lambda = 45.3$)	Sum average ($w = 7$)
$F_{1,2}^{TZ}$	F_{1}^{TZ}	F_{2}^{TZ}
Gabor ($\theta = 2.35$, $\lambda = 45.3$)	Gabor ($\theta = 2.75$, $\lambda = 45.3$)	**Gabor ($\theta = 1.18$, $\lambda = 22.6$)**
Gabor ($\theta = 1.94$, $\lambda = 5.7$)	**Gabor($\theta = 0$, $\lambda = 2.8$)**	T2w MRI intensity
Haar diagonal coefficient	Gabor ($\theta = 0.79$, $\lambda = 11.3$)	**Gabor ($\theta = 2.75$, $\lambda = 45.3$)**
Gabor ($\theta = 0$, $\lambda = 11.3$)	Gabor ($\theta = 1.57$, $\lambda = 11.3$)	**Info. measure 2 ($w = 5$)**
Gabor ($\theta = 0$, $\lambda = 5.7$)	Gabor ($\theta = 2.36$, $\lambda = 8.2$)	**Gabor ($\theta = 1.57$, $\lambda = 45.3$)**
Energy ($w = 5$)	Intensity range ($w = 5$)	Gabor ($\theta = 2.75$, $\lambda = 45.3$)
Inverse diff. moment ($w = 5$)	Gabor ($\theta = 1.57$, $\lambda = 2.8$)	**Gabor ($\theta = 0$, $\lambda = 45.3$)**
Gabor ($\theta = 1.18$, $\lambda = 8.2$)	Gabor ($\theta = 1.57$, $\lambda = 5.7$)	Intensity mean ($w = 3$)
Gabor ($\theta = 1.57$, $\lambda = 2.8$)	Sobel horizontal edge	**Gabor ($\theta = 1.57$, $\lambda = 22.6$)**
Diagonal edge descriptor	Diagonal edge descriptor	Diagonal edge descriptor
$F_{1,2}^{ALL}$	F_{1}^{ALL}	F_{2}^{ALL}
Entropy ($w = 5$)	Sum entropy ($w = 3$)	Sum variance ($w = 7$)
Gabor ($\theta = 1.57$, $\lambda = 11.3$)	**Gabor ($\theta = 2.75$, $\lambda = 2.8$)**	Sum entropy ($w = 7$)
Gabor ($\theta = 1.57$, $\lambda = 22.6$)	**Gabor ($\theta = 2.36$, $\lambda = 11.3$)**	Sum variance ($w = 5$)
Gabor ($\theta = 1.57$, $\lambda = 11.3$)	Gabor ($\theta = 1.18$, $\lambda = 22.6$)	Sum entropy ($w = 5$)
Gabor ($\theta = 2.75$, $\lambda = 11.3$)	**Gabor ($\theta = 0.39$, $\lambda = 11.3$)**	Sum average ($w = 5$)
Gabor ($\theta = 2.75$, $\lambda = 22.6$)	Gabor ($\theta = 2.36$, $\lambda = 8.2$)	Info. measure 1 ($w = 5$)
Kirsch edge descriptor 3	Kirsch edge descriptor 1	Diff. variance ($w = 5$)
Kirsch edge descriptor 2	Gabor ($\theta = 0.39$, $\lambda = 22.6$)	Sum average ($w = 7$)
Gabor ($\theta = 2.36$, $\lambda = 8.2$)	Gabor ($\theta = 1.57$, $\lambda = 11.3$)	Info. measure 1 ($w = 7$)
Diagonal edge descriptor	Kirsch edge descriptor 3	Sum average ($w = 3$)

Table 4

For all combinations of training and testing datasets, the mean AUC for TZ and PZ cancer detection is shown for the zone-aware (C^{TZ} and C^{PZ}) and zone-ignorant (C^{ALL}) classifiers. Two-sample *t*-tests were used to evaluate the statistical significance of differences in AUC between zone-aware and zone-ignorant classifiers.

	TZ Cancer Detection			PZ Cancer Detection		
	AUC (C^{TZ})	**AUC (C^{ALL})**	***p*-value**	**AUC (C^{PZ})**	**AUC (C^{ALL})**	***p*-value**
Trained on I1 (40)						
$C_{1\rightarrow1}$	**.58**	**.58**	.93	**.61**	.51	.05
$C_{1\rightarrow2,2^*}$	.63	**.66**	.62	**.68**	.27	<.001
$C_{1\rightarrow3}$	.59	.56	.84	**.56**	.41	.19
Trained on I2 (11)						
$C_{2\rightarrow2}$	**.58**	**.58**	.97	**.70**	.31	<.01
$C_{2\rightarrow2^*}$	.54	**.61**	.33	**.66**	.19	<.001
$C_{2\rightarrow1}$	**.57**	**.57**	.96	**.60**	.50	.02
$C_{2\rightarrow3}$	**.64**	.53	.27	**.58**	.38	.09
Trained on I1+I2 (51)						
$C_{1,2\rightarrow1}$	.58	**.59**	.85	**.63**	.49	<.01
$C_{1,2\rightarrow2}$	**.61**	.60	.90	**.71**	.33	<.01
$C_{1,2\rightarrow2^*}$	**.68**	.59	.46	**.64**	.18	<.001
$C_{1,2\rightarrow3}$	**.57**	**.57**	.98	**.54**	.41	.30

2* refers to 16 patients from St. Vincent's Hospital who did not undergo radical prostatectomy